Model of the Lateral Distribution of the Radio Emission from Air Showers in the 70–350 MHz Frequency Band

Alan Coleman[a,*]

[a]*Bartol Research Institute, Dept. of Physics and Astronomy, University of Delaware, 104 The Green, 19716 Newark, USA*

E-mail: alanc@udel.edu

The radio emission from air showers is beamed forward during shower development and produces a characteristic footprint on the ground. This emission imprints the content of electromagnetic particles in the cascade and, via measurements with radio antennas, can be used to study cosmic ray and particle physics. Compared to that of particle detectors, the radio footprint is more complex, generally including a Cherenkov ring as well as azimuthal asymmetries in the shower plane due to interference. Understanding the structure of this emission and the footprint of the ground is important for an accurate description of the electromagnetic content in air showers and has been used directly in likelihood-based reconstructions. In this work, we describe an analytical model for the distribution of signal in the frequency band from 70–350 MHz based on CoREAS simulations for the South Pole location. We model both the geomagnetic and charge excess emissions in this band and characterize the evolution of the respective footprints for showers which reach a maximum size both above and below ground.

---

*Speaker

1. Introduction

Ultra-high energy cosmic rays that interact in the upper atmosphere create particle cascades known as *air showers*. The majority of the particles in an air shower are *electromagnetic* particles (γ and e$^\pm$), with subdominant contributions from muons and hadrons. The bulk motion of the $e^\pm$ particles during the development produces radio-frequency (RF) emission. Due to the $O(1\text{m})$ thickness of the shower front, this emission is coherent in the radio band and is beamed in the forward direction.

The RF emission from an air shower is caused by two effects. The dominant one is the *geomagnetic effect*, a result of the opposite sign of the Lorentz force for positrons and electrons moving in Earth's magnetic field ($\vec{B}$). This separation of charge induces a current and produces photons with a polarization in the $\hat{v} \times \hat{B}$ direction for a shower propagating in the $\hat{v}$ direction. The subdominant effect is known as *charge excess* emission (also called Askaryan emission) [1]. During development, the additional electrons liberated from molecules in the atmosphere result in a changing net charge within the shower front. The charge excess emission is polarized in the radial direction with respect to $\hat{v}$. On the ground, the interference pattern that is created by these two effects results in a footprint that is not rotationally symmetric about the shower axis and also depends on the details of the shower development and altitude at which it is observed.

The electromagnetic radiation can be measured using $\geq 1\,\text{km}^2$ arrays of antennas. Leveraging the structure of the air shower footprint, properties of the air showers can be reconstructed. Due to the production mechanisms being a result of the motion of $e^\pm$, the energy content of the electromagnetic particles in the shower can be sampled using radio antennas [2]. Additionally, the slant depth into the atmosphere at which the shower reaches maximum size, X_max, can also be identified [3–5]. The latter quantity is correlated with the mass of the cosmic ray that initiated the air shower.

Extracting these quantities requires a good model of how both the energy and X_max affect the lateral distribution of RF fluence (radiated energy per area) on the ground. Previous work has focused on developing a lateral distribution function (LDF) for the energy fluence in the 30–80 MHz frequency band for vertical [6] and horizontal [7] air showers. Due to the differing nature of the emission mechanisms, the LDF has been studied separately for the geomagnetic and charge excess footprints. In this scheme, the two LDFs can then be combined, taking into account the interference, to produce a complete model for the lateral distribution of emission.

Several experiments such as the Square Kilometer Array [8, 9], the Radar Echo Telescope [10], and the IceTop Surface Enhancement [11] of the IceCube Neutrino Observatory [12, 13] will be working in a higher frequency band, up to several hundred MHz. In this work, we will be applying the method of developing an LDF model for the two emission mechanisms in the 70–350 MHz frequency band for use at the South Pole. We present a signal model which can describe the spatial distribution of the energy fluence from air showers as a function of the slant depth from X_max to the observation level, dX_max, and an overall scaling.

2. Lateral Distribution of Signal

To study the emission from cosmic-ray air-showers, a set of simulations was created. The Monte Carlo simulation of the air showers was produced using CORSIKA v7.7401 [14] and the
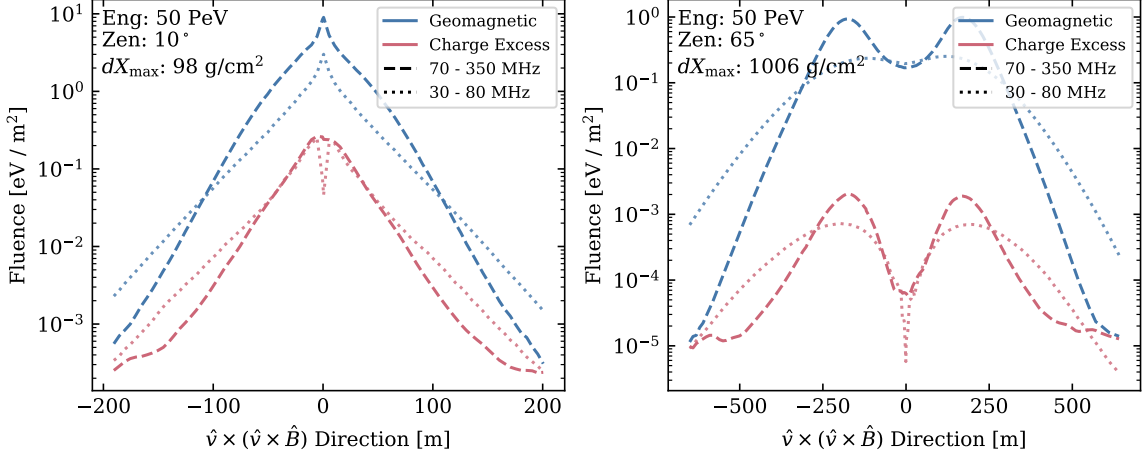
Figure 1: The energy fluence from two simulated air showers with different dX_{max} values is show in the panels above. For each air shower, the lateral distribution of the fluence for each emission mechanism (indicated by color) is shown for two overlapping frequency bands (dashed and dotted lines). The fluence is shown as a function of distance from the shower axis along the $\hat{v} \times (\hat{v} \times \hat{B})$ direction.

radio emission was produced via the included CoREAS [15] package. SIBYLL2.3d [16] and FLUKA [17] were used as models to describe the high- and low-energy hadronic interactions, respectively, and both proton and iron primaries were generated to sample a large range of X_{max} values. Zenith angles from 0°–65° were used, generated in discrete steps of 5°, while random azimuth angles were used. The air showers were thinned at a level of 1×10^{-6} and the South Pole atmosphere (atmospheric model 33 in CORSIKA) and altitude were used.

Within CoREAS, there is no direct way to identify which portion of the total electric field is a result of a given emission process. However, one can make use of polarization of the RF emission to separate them. This is done by noting that the geomagnetic emission, being a product of the Lorentz force, is polarized along the $\hat{v} \times \hat{B}$ direction. Since the charge-excess emission is instead radially polarized, the two processes produce perpendicular emission for locations directly on the $\hat{v} \times (\hat{v} \times \hat{B})$ axis (see ref. [18, 19]). The electric fields were sampled with 5 m spacing along the $\hat{v} \times (\hat{v} \times \hat{B})$ axis out to 300 m and with 10 m spacing beyond that out to 750 m. The energy fluence for two simulated air showers is shown in fig. 1. The two emission mechanisms are shown separately, for two frequency bands. The lower band, used by several existing experiments, has a qualitatively different shape than that of the 70–350 MHz band. Of note, the emission in the 30–80 MHz frequency band exhibits a much deeper dip in the geomagnetic emission inside the Cherenkov cone (i.e. $r \lesssim 200$ m). The differing shape motivates the need for new model of the LDF for this higher frequency band.

2.1 Selection of Data

The emission from an air shower is beamed forward due to the speed at which the shower front moves and produces a cone of coherent RF light with an opening angle of $\sim 1°$. This coherent emission produces a Cherenkov ring on the ground at radii up to $O(100$ m$)$ for zenith angles below 65° at the South Pole. For larger distances from the shower axis, non-coherent emission occurs and artifacts, such as that from thinning, result in waveforms that are mostly noise. The data was
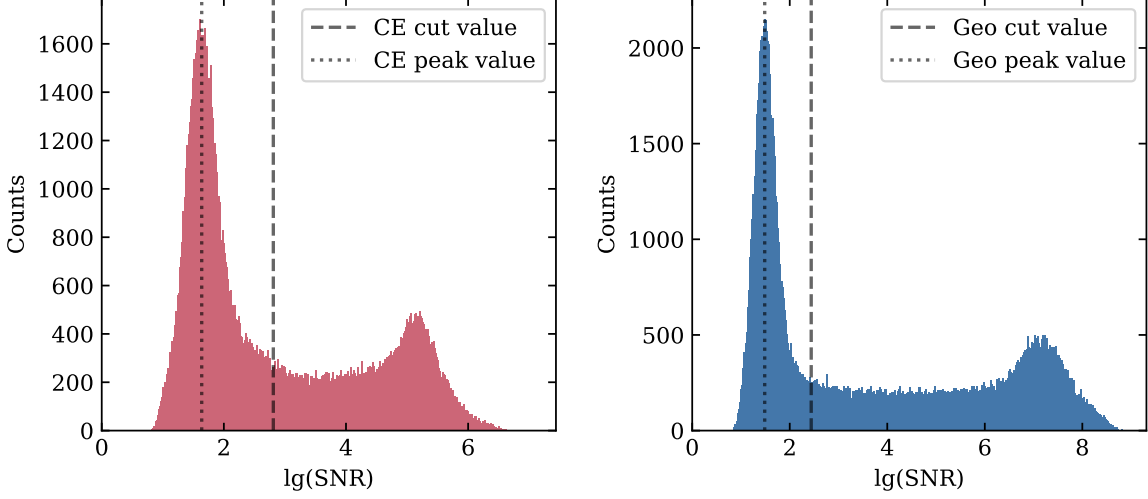
Figure 2: The distribution of SNR (see eq. (1)) values for the simulated locations along the $\hat{v} \times (\hat{v} \times \hat{B})$ axis are shown for the both emission processes. The dotted line indicates the identified low-SNR peak while the dashed line indicates the threshold value used in this analysis.

cleaned to get rid of this noise using a signal-to-noise ratio (SNR) cut where,

$$\text{SNR} = \left(\frac{|\vec{E}_i|}{\text{RMS}(|\vec{E}_i|)} \right)^2 , \tag{1}$$

for electric-field amplitudes, $\vec{E}_i$, and where the RMS is calculated only on the final third of the waveform. The distributions of SNR are shown in fig. 2. Waveforms with coherent emission make up the larger SNR values while those with low/no coherence produce the peak at small SNR values. The low-SNR peak was identified and fit to a Gaussian with mean, $\bar{x}$, and standard-deviation, Δ. In this analysis, only waveforms with SNR $> \bar{x} + 2\Delta$ are used.

2.2 Empirical Model for Emissions

For both emission mechanisms, an empirical model was chosen to describe the energy fluence for locations on the $\hat{v} \times (\hat{v} \times \hat{B})$ axis. Both are motivated by the model proposed in ref. [6] with emission being largely the sum of two Cherenkov peaks at $\pm \mu$ and with a thickness of σ. For the charge-excess emission, two skewed-Gaussians are used,

$$F_{\text{ce}}(r) = \frac{A_{\text{ce}}}{2} \left(\left(1 + \text{erf} \left[\delta \frac{r - \mu_{\text{ce}}}{\sqrt{2}\sigma_{\text{ce}}} \right] \right) \hat{G}(r, \mu_{\text{ce}}, \sigma_{\text{ce}}) + \left(1 + \text{erf} \left[\delta \frac{-r - \mu_{\text{ce}}}{\sqrt{2}\sigma_{\text{ce}}} \right] \right) \hat{G}(-r, \mu_{\text{ce}}, \sigma_{\text{ce}}) \right). \tag{2}$$

The geomagnetic emission is the sum of two Gaussians and with an additional term to fill in the values at distances close to the core,

$$F_{\text{geo}}(r) = A_{\text{geo}} \left(\hat{G}(r, \mu_{\text{geo}}, \sigma_{\text{geo}}) + \hat{G}(-r, \mu_{\text{geo}}, \sigma_{\text{geo}}) + \frac{c}{1 + \exp[5(r/\mu_{\text{geo}} - 1)]} \right). \tag{3}$$

For both models, the amplitudes A_{ce} and A_{geo} include an implicit normalization,

$$\hat{G}(r, \mu, \sigma) = \exp \left[-\frac{(r - \mu)^{p(r)}}{2\sigma^{p(r)}} \right], \qquad p(r) = \begin{cases} 2(r/\mu)^{-b/1000}, & \text{if } r > \mu \text{ and } \mu > 1\,\text{m} \\ 2r^{-b/1000}, & \text{if } r > \mu \text{ and } \mu \le 1\,\text{m} \\ 2, & \text{else.} \end{cases} \tag{4}$$
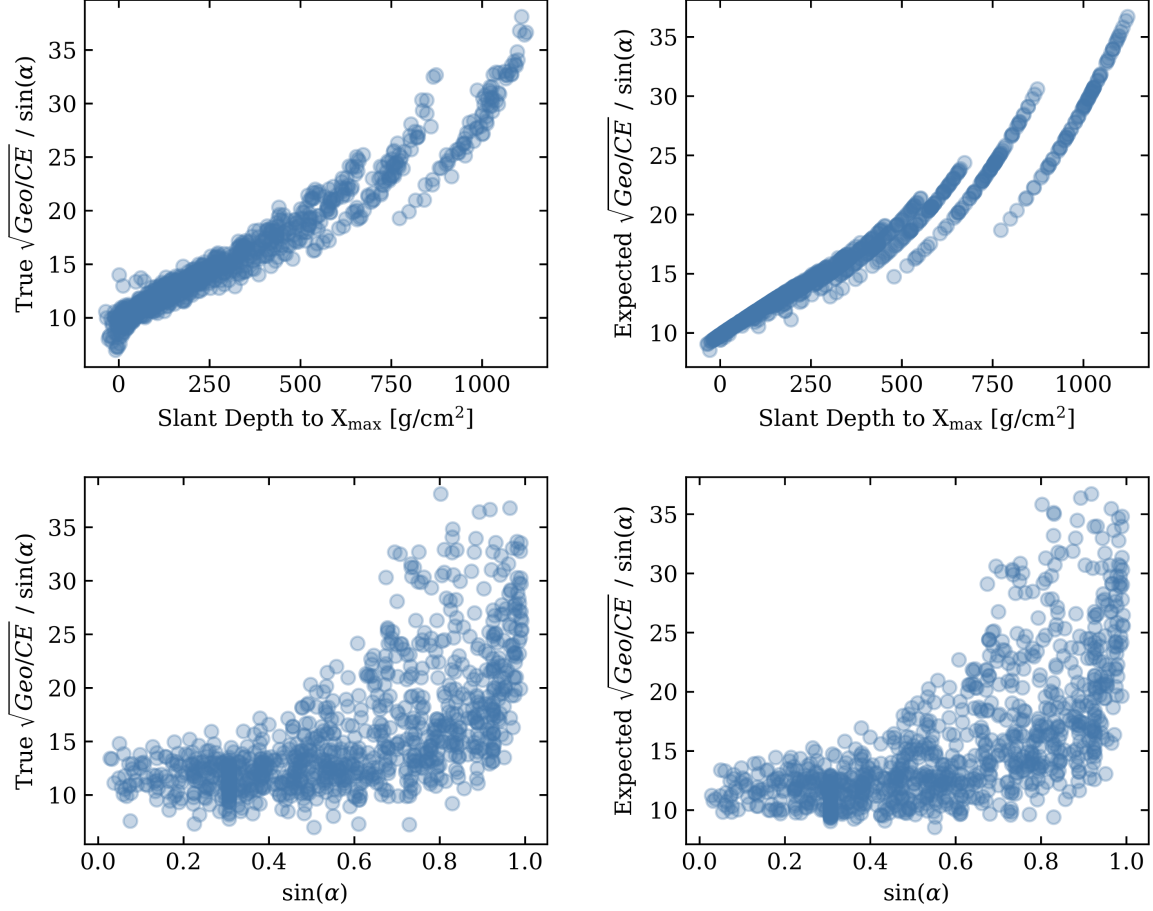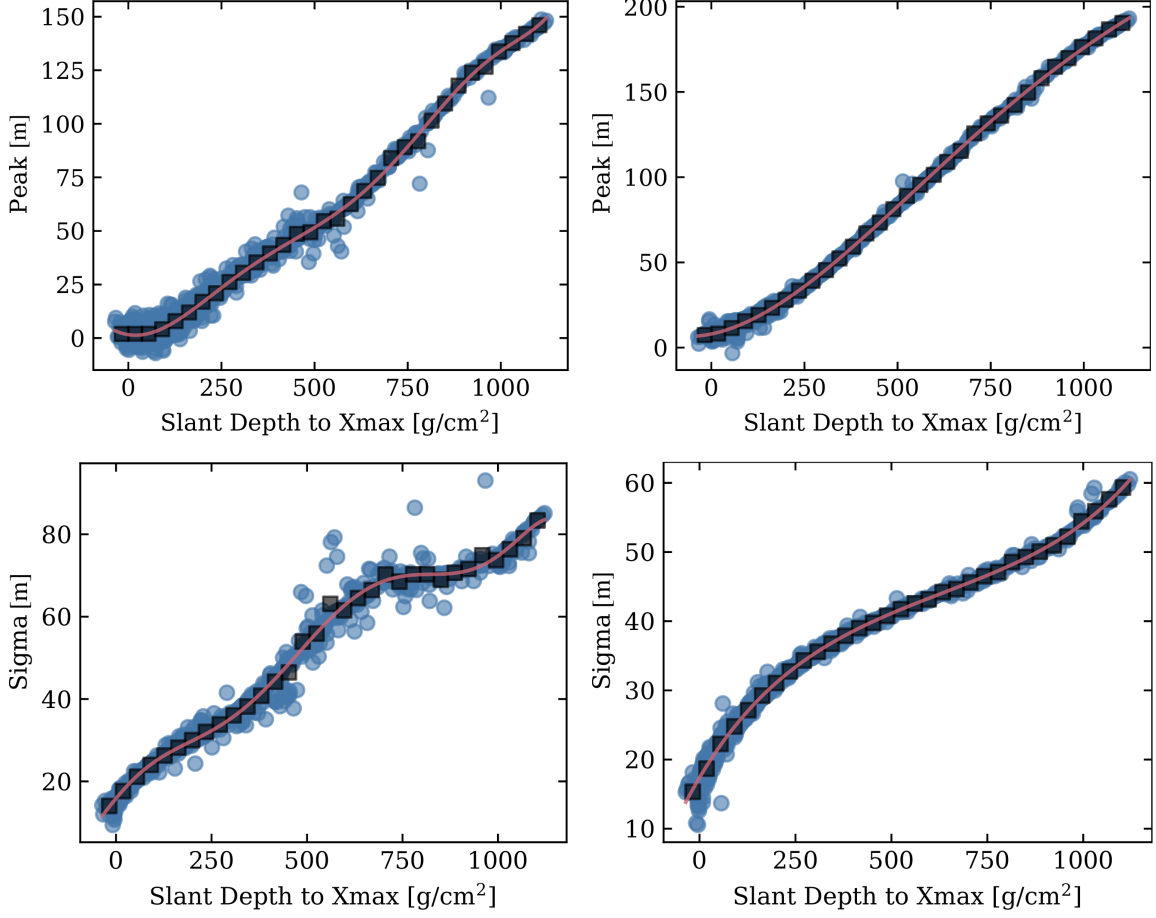
Figure 3: Left: the relationship between the total energy emitted via the geomagnetic and charge-excess processes in the 70–350 MHz frequency band for simulated air showers. This is shown as a function of dX_{max} (top) and $\sin(\alpha)$ (bottom). Right: the same quantities as for the events on the left, but as calculated by the model in eq. (5).

The b factor increases the Gaussian slope which falls off faster than $\exp(-r^2)$ outside of the Cherenkov ring. For eqs. (2) and (3), the values of μ and σ are not necessarily the same and both include a normalization, A_{ce} and A_{geo}, respectively.

2.3 Relative Emission Strength

While the two components can be fit separately, to eventually combine them, a model for the relative signal strength must be included. By numerically integrating each simulation, the total fluence for each component was calculated. In a previous study for the South Pole location, the electric field amplitude of the geomagnetic emission was shown to evolve with $\sin(\alpha)$ near the Cherenkov ring [20] where α is the angle between $\hat{v}$ and $\hat{B}$. Following this, the energy fluence was converted to a field-strength equivalent quantity and scaled, $\bar{R} = \sqrt{A_{geo}/A_{ce}}/\sin(\alpha)$. This quantity is shown in the left panels of fig. 3. A model was tuned to describe the relative emission as a function of the zenith angle (θ) and dX_{max},

$$\bar{R} = (a_0 + a_1 \, dX_{max} + a_2 \, (dX_{max})^2 + a_3 \, (dX_{max})^3)(1 + b_1 \, \sec(\theta) + b_2 \, \sec^2(\theta) + b_3 \, \sec^2(\theta)), \quad (5)$$

5

Figure 4: The evolution of the parameters μ (top) and σ (bottom) from the charge-excess LDF eq. (2) and geomagnetic LDF eq. (3) (left and right, respectively) are shown as a function of $dX_{\max}$. The best-fit parameters of individual simulated showers are shown in blue circles, the binned values are shown in black squares and a polynomial fit is shown by the red line.

where the parameters $\{a_i, b_i\}$ were fit such that they best describe the ratio for all simulated showers. The agreement between the model and the data is better than 5%.

2.4 Complete Model of the LDF

Using eqs. (2) and (3), the fluence for both emission components were fit, leaving all parameters free. The evolution of each parameter as a function of $dX_{\max}$ was then studied. The peak and the spread for both emission processes are shown in fig. 4. These parameters describe the radius and thicknesses of the Cherenkov ring and increase with distance to the shower maximum. This is consistent with the simplistic image of an increasingly distant source with beamed emission at a particular angle and is also consistent with previous work in other frequency bands [6, 7]. The evolution is fit to polynomials in $dX_{\max}$ as part of the parameterization.

Combining all of the pieces above, the full description of the LDF is constructed by taking into
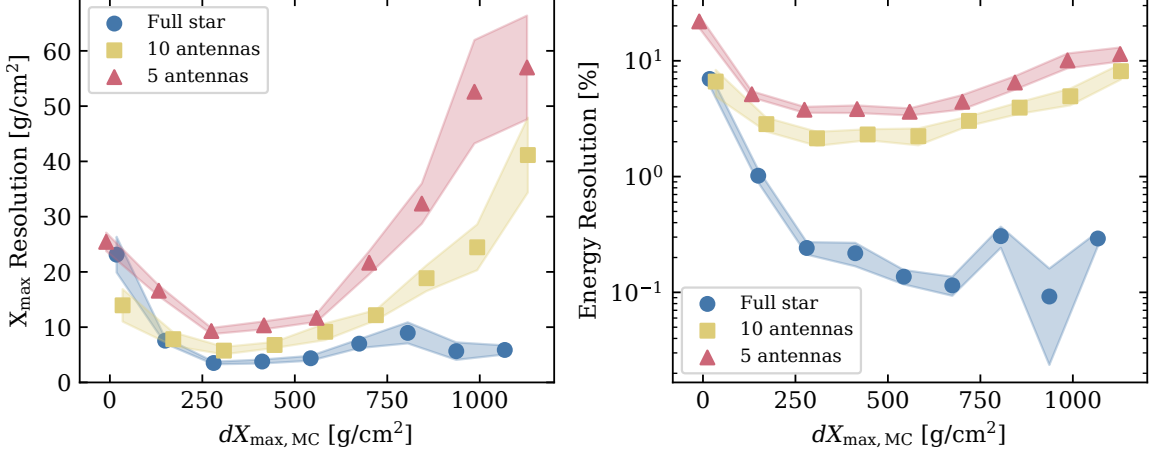
Figure 5: Quality of the reconstruction for simulated air showers on a star-pattern (circles) and for a hexagonal array with 75 m spacing (square/triangles). The resolution on X_{max} and total radiated energy in the 70–350 MHz band is shown as a function of the distance to X_{max}, dX_{max}.

account the polarization of the two emission components,

$$F_{\hat{v} \times \hat{B}}(r, \phi, dX_{max}) = A_{tot} \left(\sqrt{F_{geo}(r, dX_{max})} + \cos\phi \sqrt{F_{ce}(r, dX_{max})} \right)^2$$
$$F_{\hat{v} \times (\hat{v} \times \hat{B})}(r, \phi, dX_{max}) = A_{tot} \sin^2\phi F_{ce}(r, dX_{max}),$$
(6)

where ϕ is the polar angle in the $\hat{v} \times \hat{B}$ coordinate system. The amplitudes of the emission components are fixed using eq. (5), $A_{geo} \longrightarrow A_{geo} k/(k+1)$ and $A_{ce} \longrightarrow A_{ce}/(k+1)$ where $k = \bar{R}^2 \sin^2(\alpha)$ and the total amplitude is given by A_{tot}. Likewise, the functional forms F_{ce} and F_{geo} are extended to be functions also of dX_{max} via, e.g., $\mu \longrightarrow \mu(dX_{max})$, as described previously.

3. Reconstruction Potential

As a final test of the quality of how well eq. (6) describes the complete air shower footprint, an additional air-shower library was used to generate the electric fields arriving at antennas for two array layouts. As a best-case scenario, the total fluence was reconstructed using a star-shaped pattern with eight equally-spaced radial spokes. As a more realistic test, air showers were randomly simulated on a hexagonal array with 75 m spacing using the interpolation process described in [21]. In this second test, the antennas locations with the five- and ten-largest fluences were kept for the reconstruction. During the reconstruction, A_{tot} and dX_{max} were left as free parameters in the fit and the true core and zenith angle were used.

A comparison between the reconstructed and true values is shown in fig. 5. The resolution on X_{max} is about 5–25 g/cm² in the ideal case with the best resolution for $dX_{max} > 250$ g/cm². For the more realistic cases, the resolution is slightly worse for $dX_{max} < 600$ g/cm² but gets very large for distant air showers. Meanwhile, the energy resolution is less than 10% in for air showers when using ten antennas in the reconstruction.

4. Conclusions

We presented a model of the spatial distribution of air-shower fluence for the 70–350 MHz frequency band. This model separately describes the charge excess and geomagnetic emission contributions as well as the way that the shape evolves with dX_{max}. The full model can thus be used to generate the expected energy fluence given a total radiated energy and X_{max} (or equivalently dX_{max}). As a basic test of the application of this model, simulated air-shower events were reconstructed. The resolution on X_{max} is not competitive with current methods [3–5], particularly at high dX_{max}. However, the energy resolution, $\leq 10\%$, is comparable to other methods including that of fluorescence detector measurements.

Acknowledgements

References

[1] G. A. Askar'yan *Zh. Eksp. Teor. Fiz.* **41** (1961) 616–618.

[2] **Pierre Auger** Collaboration, A. Aab *et al. Phys. Rev. D* **93** no. 12, (2016) 122005.

[3] **LOFAR** Collaboration, S. Buitink *et al. Phys. Rev. D* **90** no. 8, (2014) 082003.

[4] P. A. Bezyazeekov *et al. Phys. Rev. D* **97** no. 12, (2018) 122004.

[5] A. Corstanje *et al. Phys. Rev. D* **103** no. 10, (2021) 102006.

[6] C. Glaser, S. de Jong, M. Erdmann, and J. R. Hörandel *Astropart. Phys.* **104** (2019) 64–77.

[7] F. Schlüter and T. Huege *arXiv preprint arXiv:2203.04364* (2022) .

[8] "The Square Kilometer Array." http://www.skao.int.

[9] T. Huege *et al. EPJ Web Conf.* **135** (2017) 02003.

[10] **Radar Echo Telescope** Collaboration, S. Prohira *et al. Phys. Rev. D* **104** no. 10, (2021) 102006.

[11] **IceCube** Collaboration, F. G. Schröder *et al. PoS* **ICRC2019** (2020) 418.

[12] **IceCube** Collaboration, R. Abbasi *et al. Nucl. Instrum. Meth. A* **700** (2013) 188–220.

[13] **IceCube** Collaboration, M. G. Aartsen *et al. JINST* **12** no. 03, (2017) P03012.

[14] D. Heck *et al. Report FZKA 6019* (1998) .

[15] T. Huege, M. Ludwig, and C. W. James *AIP Conf. Proc.* **1535** no. 1, (2013) 128.

[16] F. Riehn *et al. Phys. Rev. D* **102** no. 6, (2020) 063002.

[17] A. Ferrari, P. R. Sala, A. Fasso, and J. Ranft *INFN/TC* **5** (2005) ll.

[18] T. Huege *Phys. Rept.* **620** (2016) 1–52.

[19] F. G. Schröder *Prog. Part. Nucl. Phys.* **93** (2017) 1–68.

[20] E. N. Paudel, A. Coleman, and F. G. Schroeder *Phys. Rev. D* **105** no. 10, (2022) 103006.

[21] **IceCube** Collaboration, R. Abbasi *et al. JINST* **17** no. 06, (2022) P06026.